ATP-triggered $Fe(CN)_2CO$ synthon transfer from the maturase HypCD to the active site of apo-[NiFe]-hydrogenase

Anna Kwiatkowksi[1], Giorgio Caserta[1*], Anne-Christine Schulz[1], Stefan Frielingsdorf[1], Vladimir Pelmenschikov[1], Kilian Weisser[2], Adam Belsom[3], Juri Rappsilber[3,4,5], Ilya Sergueev[6], Christian Limberg[2], Maria-Andrea Mroginski[1], Ingo Zebger[1] and Oliver Lenz[1*]

[1] Institut für Chemie, Technische Universität Berlin, Straße des 17. Juni 135, 10623 Berlin, Germany

[2] Institute of Chemistry, Humboldt-Universität zu Berlin, Brook-Taylor-Straße 2, 12489 Berlin, Germany

[3] Institute of Biotechnology, Chair of Bioanalytics, Technische Universität Berlin, Gustav-Meyer-Allee 25, 13355 Berlin, Germany

[4] Si-M/'Der Simulierte Mensch', a Science Framework of Technische Universität Berlin and Charité – Universitätsmedizin Berlin, 10623 Berlin, Germany

[5] Wellcome Centre of Cell Biology, University of Edinburgh, Edinburgh EH9 3BF, UK

[6] Deutsches Elektronen-Synchrotron, Notkestraße 85, 22607 Hamburg, Germany

*Corresponding authors

Abstract

[NiFe]-hydrogenases catalyze the reversible activation of H_2 using a unique $NiFe(CN)_2CO$ metal site, which is assembled by a sophisticated multi-protein machinery. The [4Fe–4S]-cluster-containing HypCD complex, which possesses an ATPase activity with an hitherto unknown function, serves as the hub for the assembly of the $Fe(CN)_2CO$ sub-fragment. HypCD is also thought to be responsible for the subsequent transfer of the iron fragment to the apo-form of the catalytic hydrogenase subunit, but the underlying mechanism remained unexplored. Here, we performed a thorough spectroscopic characterization of different HypCD preparations using infrared, Mössbauer and NRVS spectroscopy, revealing molecular details of the coordination of the $Fe(CN)_2CO$ fragment. Moreover, biochemical assays in combination with spectroscopy, AlphaFold structure predictions, protein-ligand docking calculations and crosslinking MS deciphered unexpected mechanistic aspects of the ATP requirement of HypCD, which we found to actually trigger the transfer of the $Fe(CN)_2CO$ fragment to the apo-hydrogenase.

Introduction

By making use of earth-abundant nickel and iron ions, [NiFe]-hydrogenases catalyze the reversible activation of H_2 close to the thermodynamic potential under ambient conditions [1]. The functional unit of [NiFe]-hydrogenases features a bipartite architecture consisting of a catalytically competent large subunit that carries the heterobimetallic $NiFe(CN)_2CO$ active site and a small subunit, which contains one to three Fe–S clusters as an electric wire. The synthesis and assembly of the $NiFe(CN)_2CO$ cofactor requires an intricate protein machinery comprising at least six Hyp proteins named HypA-F [2–5]. The current biosynthesis model envisages the [4Fe–4S] cluster-containing HypCD protein complex as a hub for the assembly of the $Fe(CN)_2CO$ synthon of the catalytic site (Supplementary **Fig. S1**). The CN^- strong field ligands are synthesized from carbamoylphophate by the maturases HypF and HypE [6] and are supposed to be transferred by the latter to a single iron ion transiently bound by HypCD. The aerobic biosynthesis of the CO ligand from N^{10}-formyl-tetrahydrofolate has recently been uncovered [7,8], while the corresponding anoxic pathway remains elusive [9,10]. The assembled $Fe(CN)_2CO$ synthon is then transferred to the apo-form of the large hydrogenase subunit via an unknown mechanism. Only then do the maturases HypA and HypB complete the active site metalation by mediating the insertion of a Ni ion [11]. Finally, the fully metalated hydrogenase large subunit is usually processed by endoproteolytic cleavage of its C-terminal extension [12–14]. This step has been shown to trigger structural changes at the NiFe site (e.g. incorporation of an OH ligand bridging Ni and Fe [15]), which also allows the association of the large and small subunits to form catalytically competent [NiFe]-hydrogenase [13].

Although the biosynthesis of the NiFe site has been examined in great detail [15,16], several aspects of the maturation process are still unclear. Among them, the mechanism by which the $Fe(CN)_2CO$ fragment is synthesized and then safely transferred from the HypCD complex to the apo-large subunit is essentially unknown. Furthermore, recent work from the Sawers´ group has revealed an unexpected ATPase activity of the HypCD complex [17,18]. However, neither an obvious ATP binding site, nor a biological function of the hydrolytic activity have been shown. In the present study, we extend our knowledge of [NiFe]-hydrogenase maturation with new aspects. We developed *in vitro* assays with purified HypCD from *Escherichia coli* and the apo-large subunit HoxC of the regulatory [NiFe]-hydrogenase (RH) from *Cupriavidus necator* to investigate the role of the ATPase activity of HypCD in hydrogenase maturation. Based on biochemical and spectroscopic analyses supported by DFT, AlphaFold-based structure predictions, crosslinking mass spectrometry (crosslinking MS) and protein-ligand docking data, we were able to decipher the predicted binding site for ATP in HypCD as well as molecular

details that allow for the transfer of the $Fe(CN)_2CO$ synthon to the apo-form of the hydrogenase large subunit.

Results

Isolation and spectroscopic characterization of the HypCD and HoxC proteins

Holo- and apo-HypC$_{Strep}$-HypD protein complexes (Strep-tag II C-terminally fused to HypC hereafter referred to as holo- and apo-HypC$_S$-D) were isolated by Strep-Tactin-based affinity chromatography from soluble extracts (Supplementary **Table S1**) of aerobically cultivated *E. coli* (*Ec*) cells carrying pTHypDC$_{Strep}$ and pTHypDEFC$_{Strep}$ expression plasmids (Supplementary **Table S2**) [19,20]. SDS-PAGE analysis of the isolated protein complexes showed the typical bands for HypC and HypD (Supplementary **Fig. S2**), which is consistent with previous studies [19]. Apo-$_{Strep}$HoxC (apo-$_S$HoxC; Strep-tag II N-terminally fused to HoxC) from *Cupriavidus necator* (*Cn*) was heterologously overproduced in *E. coli* cells bearing the expression plasmid pTS17 (Supplementary **Table S2**) and also isolated via Strep-Tactin-based affinity chromatography. The isolated protein (complexes) were characterized by infrared spectroscopy in the 2150–1800 cm^{-1} range to verify the presence of CO and CN ligands usually observed in hydrogenase maturation intermediates and fully assembled [NiFe]-hydrogenases [1,15]. Clear IR absorption signals were exclusively detected for holo-HypC$_S$-D (Supplementary **Fig. S3**).The observed ν_{CN} signals at 2098 and 2072 cm^{-1}, and ν_{CO} signals at 1951 and 1963 cm^{-1}, resemble those previously reported [20,21], suggesting the isolation of a native-like HypCD complex. The metal content of HypC$_S$-D was then determined by inductively coupled plasma-optical emission spectroscopy (ICP-OES). The iron content of holo-HypC$_S$-D was determined with 6.64 ± 0.09 and that of apo-HypC$_S$-D with 5.37 ± 0.06. For unknown reasons, the total iron content of both proteins exceeds the theoretical iron content by 1-1.5 iron. Importantly, both proteins differed as expected by about one iron ion, which can presumably be assigned to the species equipped with CO/CN ligands (see below). To test whether both HypD and HypC are required for assembly and binding of the $Fe(CN)_2CO$ fragment, we purified the two proteins independently, and the corresponding IR measurements did not reveal any detectable CO/CN absorptions (Supplementary **Fig. S4**). These data, therefore, strongly suggest that exclusively the assembled holo-HypCD complex carries the $Fe(CN)_2CO$ fragment.

Characterization of the $Fe(CN)_2CO$ fragment in HypCD

The $Fe(CN)_2CO$ fragment of the hydrogenase active site has been shown to be EPR-silent, which has been interpreted as a Fe^{II} low-spin configuration [1]. Previous Mössbauer data on holo-HypCD revealed traces of resonance signals attributed to a low-spin Fe^{II} species, but their origin

was not confirmed by measurements on an apo-HypCD construct without the $Fe(CN)_2CO$ synthon [22]. Therefore, we recorded zero-field Mössbauer spectra for both apo- and holo-HypCs-D enriched with ^{57}Fe (see Methods). Resonance signals of both samples were simulated with different spectral components, which are shown in **Fig. 1a**,**b**. The main signals in both holo- and apo-HypCs-D are typical of a quadrupole doublet consisting of two components, each representing a $Fe^{2.5+}$-$Fe^{2.5+}$ pair of a $[4Fe–4S]^{2+}$ cluster. The isomer shifts and quadrupole splitting parameters are listed in Supplementary **Table S3.** The parameters of the [4Fe–4S] cluster in both apo- and holo-HypCs-D are almost identical to those previously reported[22], showing that the correct incorporation of the [4Fe–4S] cluster in HypCD also occurs under aerobic conditions[23]. Besides minor signals of a $[3Fe–4S]^+$ species [24], the fit used to simulate the apo-HypCs-D spectrum did not require any additional spectral components. In contrast, holo-HypCs-D contains an additional and significant resonance characterized by an isomer shift of $\delta = 0.25$ mm s^{-1} and a quadrupole splitting of $\Delta E_Q = 1.60$ mm s^{-1}. For [NiFe]-hydrogenases, these parameters have been associated with a fivefold coordinated low-spin Fe^{II} species equipped with one CO and two CN^- ligands [22,25]. The intensity of this resonance appears considerably higher than that previously reported [22], indicating a significantly higher (^{57}Fe) occupancy of the low-spin Fe^{II} species in our protein preparations.

To shed light on the coordination of the iron ions, we employed nuclear resonance vibrational spectroscopy (NRVS). This synchrotron technique provides vibrational dynamics for Mössbauer-active nuclei, such as the ^{57}Fe isotope. Typical NRVS spectra of [NiFe]-hydrogenases comprise dominant Fe–S stretching and bending modes (100–420 cm^{-1}) of the [Fe–S] clusters of the small subunit as well as Fe–CO/CN stretching and bending modes of the NiFe active site (400–650 cm^{-1}) [26,27] Depending on the (redox) state of the active site, modes of bridging hydride and hydroxide ligands have also been assigned [28,29]. Apo-HypCs-D predominantly showed signals that can be assigned to a [4Fe–4S] cluster (**Fig. 1c**). Major bands were detected at 150 cm^{-1} (bending and breathing modes of the cluster), as well as at 275 cm^{-1}, 366 cm^{-1} and 385 cm^{-1}, which represent normal modes with predominant Fe–S stretching character. These signals appeared at positions similar to those observed for the [4Fe–4S] cluster-containing ferredoxin (D14C variant) from *Pyrococcus furiosus* [30]. Holo-HypCs-D, on the other hand, exhibited additional absorptions at 438, 501, 589 and 620 cm^{-1}, which originate from modes involving the CO/CN^- ligands of the $Fe(CN)_2CO$ synthon (see next paragraph). In conclusion, our Mössbauer and NRVS data convincingly show that holo-HypCD harbors two iron cofactors, a [4Fe–4S] cluster and a low-spin $Fe^{II}(CN)_2CO$ fragment. Strikingly, the high-frequency region of the NRVS spectrum in holo-HypCs-D resembles that of the nickel-free

maturation intermediate of the membrane-bound hydrogenase (MBH) large subunit from *C. necator* (Supplementary **Fig. S5**) [15]. This intermediate has been shown to bind a five-fold coordinated $Fe(CN)_2CO$ fragment, presumably via two of the four conserved cysteine residues of the hydrogenase active site. Given the similarity of the high-frequency spectral range of the two proteins, a comparable coordination can be inferred for the $Fe^{II}(CN)_2CO$ species in both holo-HypCD and the nickel-free large hydrogenase subunit. This scenario is in agreement with prior computational and biochemical data suggesting that the $Fe(CN)_2CO$ fragment in HypCD is coordinated by one cysteine residue from HypC and one from HypD [31,32].

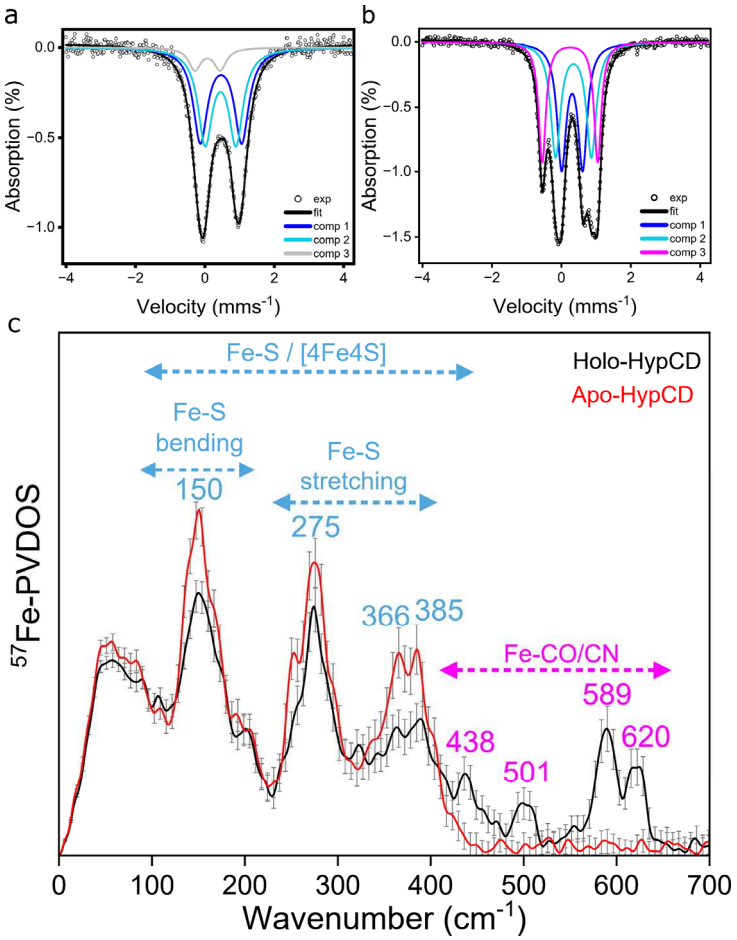

Fig. 1. Mössbauer and NRVS characterization of apo- and holo-HypCD. a-b Experimental Mössbauer data for apo- (**a**) and holo-HypCD (**b**) are depicted as single data points (circles). Black lines correspond to the curve fits containing all spectral components, the dark blue (component 1) and light blue (component 2) lines correspond to the two $Fe^{2.5+}$-$Fe^{2.5+}$ pairs of the $[4Fe–4S]^{2+}$ cluster. The grey line (component 3) in **a** represents the spectral contribution of a [3Fe–4S] cluster (minor) in apo-HypCD. The magenta line in **b** corresponds to the $Fe^{II}(CN)_2(CO)$ species in holo-HypCD. **c** NRVS spectra of apo-HypCD (red trace) showing Fe–S bending/stretching bands originating from the [4Fe–4S] cluster (blue dashed arrows). The contribution of the $Fe(CN)_2CO$ fragment is only detectable in the holo-HypCD spectrum (black trace), characterized by bands in the Fe–CN/CO region (magenta dashed arrow).

Binding site of the $Fe(CN)_2CO$ fragment in HypCD

The binding of the $Fe(CN)_2CO$ cofactor in *Ec*HypCD was further analyzed using density functional theory (DFT) calculations (see Methods). We adopted the previously proposed low-spin ferrous Fe^{II} center coordination by the thiolates of $Cys2_{HypC}$ and $Cys41_{HypD}$ (**Fig. 2a**) [31,32] as a constraint for our DFT modeling. The protein environment of the $Fe(CN)_2CO$ fragment was based on the cofactor-free AlphaFold structure of *Ec*HypCD generated as described in Methods. Notably, incorporation of the $Fe(CN)_2CO$ fragment was achieved without apparent steric clashes. Only moderate changes in the amino acid side chain positions were produced by the subsequent DFT structure optimization. The refined model of holo-*Ec*HypCD in comparison to the initial AlphaFold structure is shown in **Fig. 2a** and Supplementary **Fig. S6** (with conserved motifs of HypD highlighted). The position of the $Fe(CN)_2CO$ synthon in *Ec*HypCD is reminiscent of that in a previous model of holo-HypCD from *Thermococcus kodakarensis* (*Tk*) [31,32]. In our model, the diatomic CN^- and CO ligands form hydrogen bonds with the HypD residues His201, Gly200, and Thr149. Furthermore, Glu357 from HypD forms a hydrogen bond with the sulfur atom of Cys2 from HypC (**Fig. 2a**). The specific contacts are $(C_2)S_\gamma\cdots H–O_{\varepsilon 2}(E_{357})$ = 3.08 Å, $CN\cdots H–N_{\delta 1}(H_{201})$ = 2.87 Å, $CN\cdots H–N(H_{201}/G_{200})$ = 3.18/2.91 Å, and $CO\cdots H–O_{\gamma 1}(T_{149})$ = 2.99 Å.

The DFT model of holo-*Ec*HypCD was also used to simulate the ^{57}Fe-PVDOS (partial vibrational densities of states) contribution of the $Fe(CN)_2CO$ fragment to the NRVS spectrum discussed above and shown in **Fig. 1c**. **Fig. 2b** shows that the calculations reproduce the high-energy spectral region from 450-650 cm^{-1} well, which contains mixed modes of predominantly stretching Fe–CO/CN and bending Fe–C–O/N characters. The two modes of the strongest symmetric/antisymmetric $Fe–S(Cys2_{HypC}/Cys41_{HypD})$ stretching character were calculated at 390 and 366 cm^{-1} (Supplementary **Fig. S7**). Interestingly, these Fe–S modes of the cysteine-bound $Fe(CN)_2CO$ cofactor produce only very low ^{57}Fe-PVDOS intensities, in contrast to the corresponding vibrational energy regions of Fe–S clusters[30] such as the $[4Fe–4S]^{2+}$ cubane of HypCD (**Fig. 1c** and Supplementary **Fig. S5**). Thus, our normal mode analysis suggests that the principal Fe–S stretches of holo-*Ec*HypCD are associated with *rotations* of the FeC_3 core instead of *displacements* of the Fe center. The presence of 'NRVS-silent' Fe–S stretches in holo-*Ec*HypCD agrees well with the intensity level near the baseline around 350-400 cm^{-1} of the nickel-free hydrogenase large subunit intermediate[15] (Supplementary **Fig. S5**), which is expected to bind the $Fe(CN)_2CO$ fragment in a similar manner as HypCD (see above).

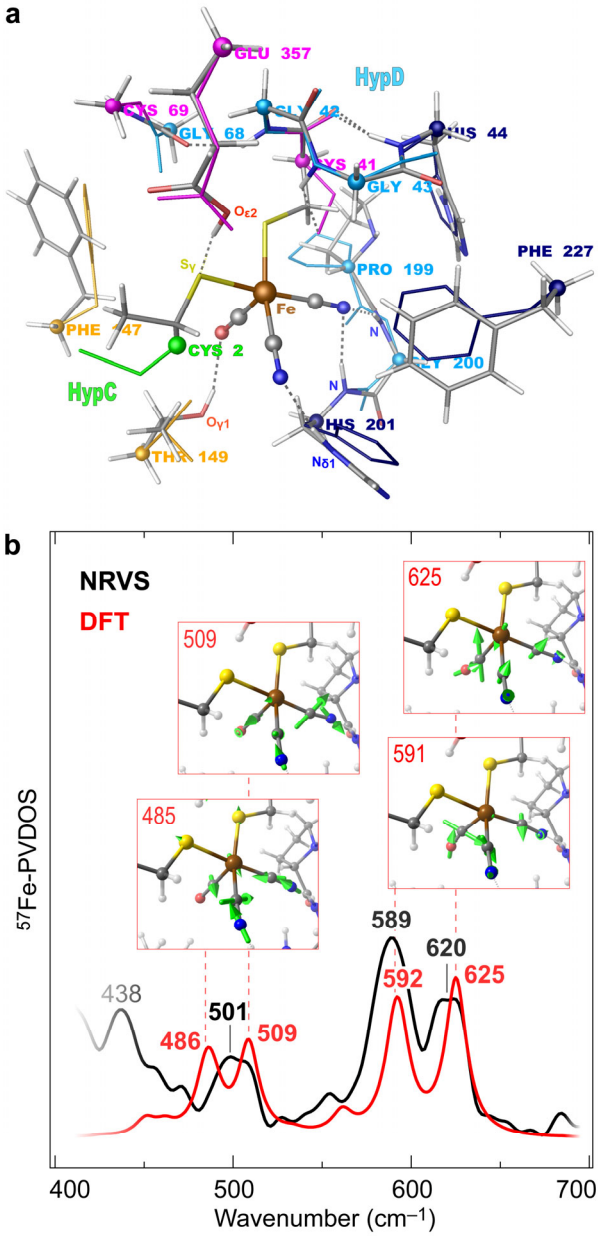

Fig. 2. **DFT modeling of the Fe(CN)$_2$CO cofactor binding site in *Ec*HypCD and the corresponding NRVS spectrum**. **a** The optimized DFT structure (tube representation, element colors) is overlaid with the original positions of the amino acid residues in the apo-*Ec*HypCD AlphaFold model (wire representation). The color codes for the reference residues of the AlphaFold model are as follows: HypC: Cys2, light green. HypD: Cys41/Cys69/Glu357, important for the assembly of the Fe(CN)$_2$CO cofactor [32,33], magenta; Phe147/Thr149 of the conserved GF$_{147}$ET$_{149}$T motif, orange; His44/His201/Phe227 matching three residues within 3 Å from the cofactor in the *Tk*HypCD model by Albareda et al.[31], dark blue; Gly42/Gly43/Gly68/Pro199/Gly200, light blue. Individual atoms participating in hydrogen bonding (···) to the cofactor are named. C$_\alpha$ and Fe(CN)$_2$CO fragment atoms are shown as spheres. **b** Predicted (DFT, red trace) and experimental (NRVS, black trace) ^{57}Fe-PVDOS of holo-*Ec*HypCD in the 400-700 cm^{-1} spectral range. Selected vibrational modes are shown in arrow-style representation above the spectra. Animations of these and other normal modes are available as part of the Supplementary **Data III**. An extended version of panel b is available as Supplementary **Fig. S7**.

ATP binding site in HypCD

Both the apo- and holo-forms of anaerobically purified HypCD and the paralogous HybG-HypD complex from *E. coli* have been shown to hydrolyze ATP [17,18]. However, the ATP binding site and the biological function of the ATPase activity remained elusive. To shed light on the possible binding site for ATP in HypCD, protein-ligand docking simulations were performed using CB-Dock2 [34,35] and the crystallographic coordinates of apo-*Tk*HypCD (PDB: 3VYR) [32]. CB-Dock2 performs docking in each cavity of the protein of interest and ranks the cavities according to the best Vina score – an empirical parameter related to the free binding energy. The more negative the score, the more reliable the result. For *Tk*HypCD, CB-Dock2 calculated five different docking sites for ATP (cavities A-E, **Fig. 3a**). Cavity A was found to have the lowest Vina score of –8.3, making it the most favorable binding site for ATP in HypCD. To test the validity of CB-Dock2, we calculated the ATP docking sites in the hydrogenase maturase HypE, which has been shown to bind and hydrolyze ATP for CN^- ligand synthesis [6]. In fact, the ATP-HypE docking data with the lowest Vina score of –8.7 corresponds to the experimentally determined binding site of the nucleotide in HypE [36] (Supplementary **Fig. S8a**,**b** and Supplementary **Table S4**). We also calculated the electrostatic charge distribution in *Tk*HypCD at pH 7.0. The surface corresponding to cavity A is strongly positively charged, making it prone to the binding of negatively charged molecules such as ATP (Supplementary **Fig. S9**). Besides determining various docking locations, CB-Dock2 also discloses the amino acid side chains surrounding the docked ligand (Supplementary **Table S5**). For cavity A, amino acid (aa) residues of both HypC and HypD are listed as connecting residues. These include $Cys38_{HypD}$ and $Cys66_{HypD}$ (*Tk* numbering, **Fig. 3b**), which have been shown to be crucial for the ATPase activity for HypCD and HybG-HypD as well as for the maturation of the hydrogenases I-III from *E. coli* [33]. The nearby residues also include the GFETT motif (residues $148\text{-}152_{HypD}$), which is highly conserved in HypDs from different species (Supplementary **Figs. S10** and **S11**). When comparing the HypCD docking data for ATP (**Fig. 3**) and the DFT model for the $Fe(CN)_2CO$ fragment (**Fig. 2a**), it appears that the same protein cleft accommodates both cofactors. In fact, Cys38 of *Tk*HypCD (analogous to Cys41 in *Ec*HypCD) is predicted to be located at hydrogen-bonding distance (ca. 3Å) from ATP (**Fig. 3b**), and its thiolate side group is proposed to be one of the two protein ligands of the $Fe(CN)_2CO$ fragment [31,32,37].

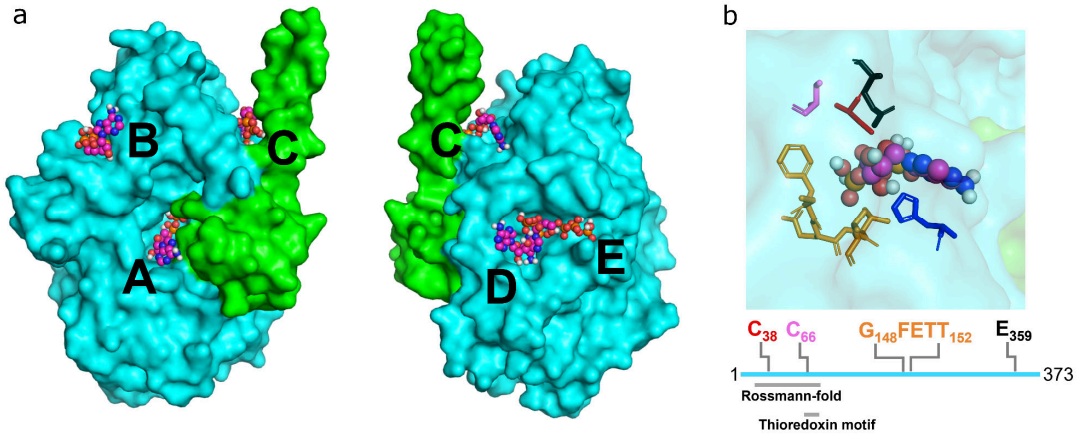

Fig. 3. Predicted docking sites for ATP in *T. kodakarensis* HypCD. a ATP-binding locations as predicted by CB-Dock2 are labelled alphabetically (A-E). Vina Scores: Cavity A: –8.3; B: –5.7; C: –6.3; D: –5.5; E: –5.9. HypD is depicted in cyan and HypC in green. ATP is shown as spheres. **b** Close-up of the predicted connection residues to ATP in cavity A, including the conserved residues Cys38 (red), Cys66 (magenta), Glu359 (black) from HypD and His45 (blue) from HypC [32,33,37,38]. The highly conserved GFETT motif (orange) in HypD (Supplementary **Figs. S10** and **S11**) is also part of cavity A, with connections to the ATP molecule. A representation of the amino acid sequence of HypD illustrates the affiliation of individual amino acid residues to the Rossman fold and/or the thioredoxin motif (grey bars) of HypD.

HypCD uses ATP to transfer the $Fe(CN)_2CO$ synthon to the apo-hydrogenase

As outlined above, CB-Dock2 data predicted a docking site for ATP in *Tk*HypCD in proximity to residues proposed to bind the $Fe(CN)_2CO$ fragment. Considering that both apo- and holo-HypCD from *E. coli* have been shown to hydrolyze ATP[17,18], it has been hypothesized that ATP might play a role either in the assembly of the $Fe(CN)_2CO$ fragment (e.g. synthesis of the CO ligand[22]) or in the transfer of the $Fe(CN)_2CO$ moiety to the apo-form of the large hydrogenase subunit. Our HypCD preparations harbor $Fe(CN)_2CO$ fragment in stoichiometric quantities and can hydrolyze ATP as shown by a biochemical (coupled) assay using pyruvate kinase (PK) and lactate dehydrogenase (LDH) and IR spectroscopy (Supplementary Note, Supplementary **Figs. S12**, **S13**). To investigate whether ATP plays role in the transfer of the $Fe(CN)_2CO$ fragment, we designed an *in vitro* assay using holo-HypCD and the apo-form of the large subunit HoxC of the regulatory hydrogenase from *C. necator*. First, we genetically replaced the C-terminal Strep-tag II at HypC in holo-HypCD with a hexa-His affinity tag (Supplementary **Table S2**), resulting into holo-$HypC_H$-D. UV-vis and IR measurements (Supplementary **Figs. S14**, **S15**) revealed almost identical spectra for holo-$HypC_H$-D and holo-$HypC_S$-D indicating that the former is fully equipped with a [4Fe–4S] cluster and the $Fe(CN)_2CO$ synthon. We then incubated holo-$HypC_H$-D, ATP (and other nucleotides, see Supplementary **Table S6**) and apo-$_S$HoxC (Strep- tag II N-terminally fused to HoxC) under anoxic conditions as detailed in the

Methods section. After incubation for 1 h, sHoxC was re-purified by Strep-Tactin affinity chromatography (**Fig. 4a,b**, Supplementary **Fig. S16**) and subsequently subjected to IR spectroscopy to verify that the $Fe(CN)_2CO$ fragment was transferred to the apo-large subunit. The results are summarized in (**Fig. 4c**). ATP turned out to be necessary for the transfer of the $Fe(CN)_2CO$ synthon. Prominent IR absorption bands were observed in HoxC when ATP was present in the reaction mixture (+ ATP), while negligible CO/CN^- signals were observed when ATP was omitted (– ATP). Such minor absorption bands were also observed for highly concentrated apo-HoxC protein solutions and are likely due to the endogenous Hyp machinery in the *E. coli* Rosetta (DE3) strain used to produce apo-HoxC. Although these data may suggest that hydrolysis of ATP is necessary for the transfer of the $Fe(CN)_2CO$ fragment to the large subunit, this does not appear to be the case, as the non-hydrolysable ATP analog β,γ-methyleneadenosine 5′-triphosphate (non-hydr. ATP) also enables efficient cofactor transfer (**Fig. 4c**). An additional control experiment with GTP (instead of ATP) also led to negligible CO/CN^- absorption bands in sHoxC and thus confirms the necessity of adenine nucleotides. Therefore, we conclude that the binding of ATP and not its hydrolysis is required to transfer the $Fe(CN)_2CO$ fragment. It is important to note that the IR spectrum of the *in vitro* matured HoxC resembles that of $preHoxG^{\Delta Ni}$ (Supplementary **Fig. S17**), a maturation intermediate of a [NiFe]-hydrogenase large subunit purified from living cells, which exclusively carries the $Fe(CN)_2CO$ unit [15]. This indicates that our *in vitro* assay enables the incorporation of the $Fe(CN)_2CO$ synthon into apo-HoxC in a native way.

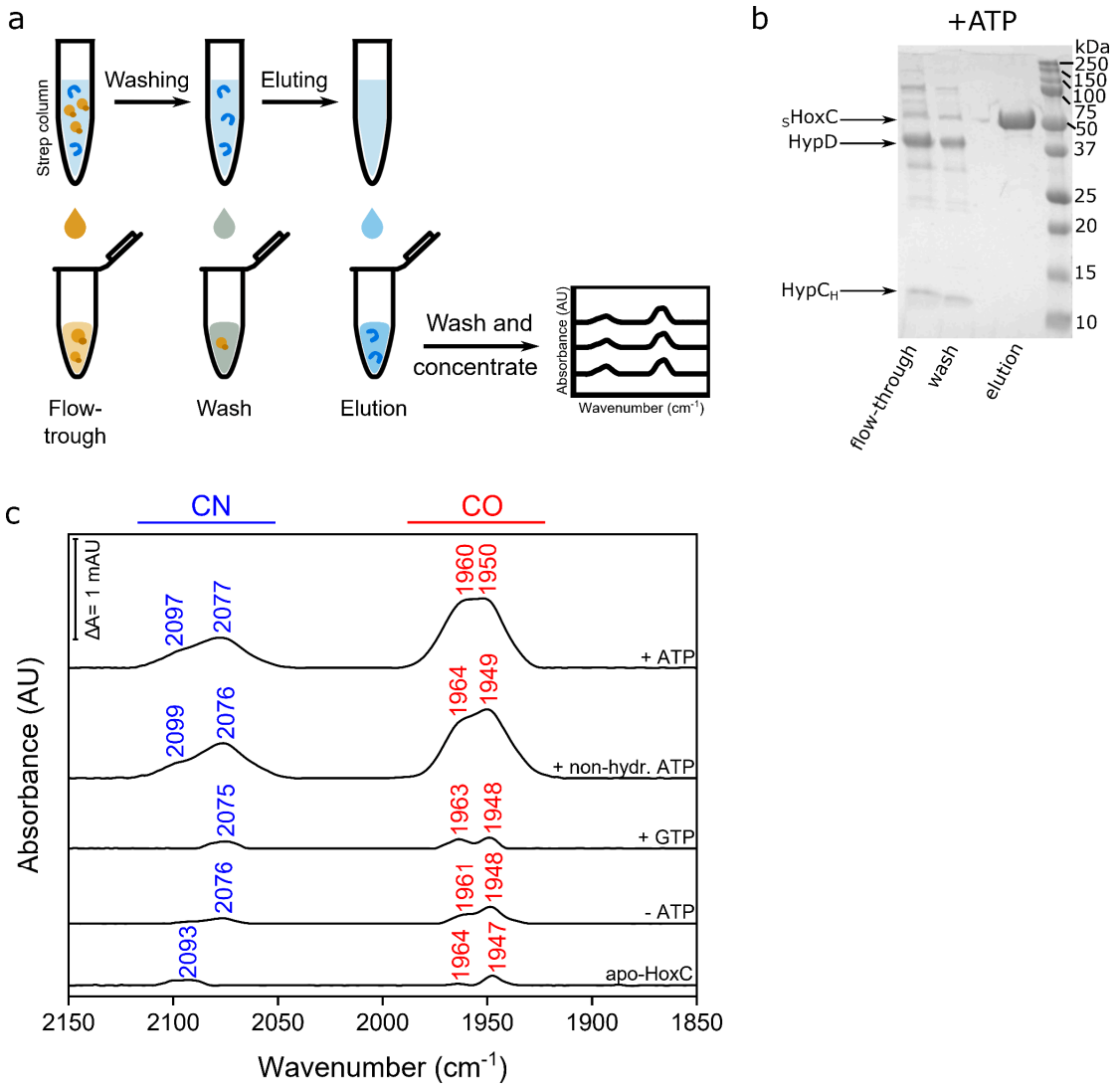

Fig. 4. ***In vitro*** **transfer assays using holo-HypCD and apo-HoxC proteins. a** Schematic representation of the $Fe(CN)_2CO$ transfer assay using holo-$HypC_H$-D (orange) and apo-$_S$HoxC (blue). **b** SDS-PAGE analysis of purified $_S$HoxC after the transfer reaction in the presence of ATP (see Supplementary **Fig. S16** for SDS-PAGE analysis for the transfer reactions with other nucleotides) and (**c**) IR spectra of purified $_S$HoxC proteins after the transfer reaction with different nucleotides. CO and CN^- absorptions in panel **c** are labelled with the corresponding wavenumbers. The spectra are normalized with respect to the amide II band intensity. Three independent experiments were performed for each transfer assay, of which one representative IR spectrum (panel **c**) and one SDS-PAGE (panel **b** and Supplementary **Fig. S16**) are shown.

ATP triggers displacements of the C-terminal part of HypC

In this study, we employed the holo-HypCD complex from *E. coli* for the *in vitro* transfer experiments. Considering the lack of an atomic structure of *Ec*HypCD, we used AlphaFold 2 to predict the protein complex. A comparison of the predicted *Ec*HypCD with the X-ray crystal structure of *Tk*HypCD (PDB: 3VYR[32]) is shown in **Fig. 5a,b**. The corresponding coordinates

are provided as part of the Supplementary Data and were also used to compute a model for the binding site of the $Fe(CN)_2CO$ fragment (**Fig. 2a**).

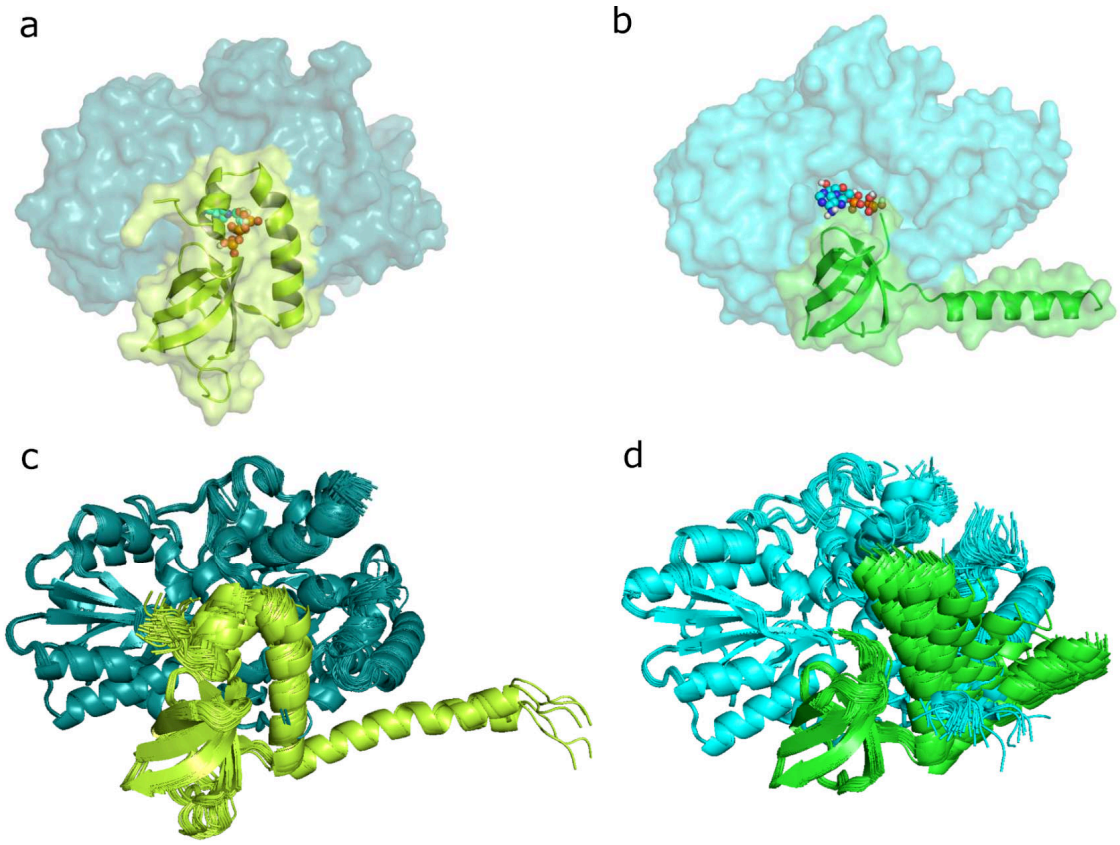

Fig. 5. **Different conformations of the C-terminal part of HypC in *Ec*HypCD and *Tk*HypCD structure predictions**. **a** AlphaFold-predicted "closed conformation" of *Ec*HypCD. The C-terminal part of HypC covers the ATP-binding pocket (ATP is shown in sphere representation). **b** "Open conformation" of the *Tk*HypCD crystal structure. The C-terminal, mostly helical part of HypC bends away from the HypCD complex, exposing the ATP/$Fe(CN)_2CO$-binding pocket. HypD is shown in **a** and **b** in the surface representation (shades of blue), while the different conformations of HypC (shades of green) are displayed in the cartoon representation for clarity. **c** Overlay representation of various structures predicted by AlphaFold 2 for *Ec*HypCD using different presettings. **d** Overlay representation of various structures predicted by AlphaFold for *Tk*HypCD using different presettings. Note, that the C-terminal part of HypC can adopt different positions, including the "open" and the "closed", while the rest of the HypCD complexes remain almost unchanged.

It has been shown that the C-terminal, mostly α-helical part (about one third of the total protein) of HypC from *T. kodakarensis* adopts different conformations when crystallized as single protein or in complex with HypD [32,37]. In case of HypC within the AlphaFold 2-predicted *Ec*HypCD complex, the C-terminal part showed a different structure and occupies a completely new position, covering the putative binding site for ATP and the $Fe(CN)_2CO$ cofactor (**Fig. 5a**). This arrangement in *Ec*HypCD, referred to here as "closed conformation", is in contrast to the "open conformation" in *Tk*HypCD with a $Fe(CN)_2CO$/ATP binding site open to the solvent

(**Fig. 5b**). AlphaFold 2 also predicted a closed conformation for the HybG-HypD complex from *E. coli* (Supplementary **Fig. S18**), which has been shown to catalyze ATP hydrolysis[18]. However, it should be noted that the reliability of the position of the C-terminal part of HypC is rather low according to the AlphaFold 2 confidence score (Supplementary **Fig. S19**), indicating a certain flexibility of this structural element. To further evaluate the structural differences of the HypCD complexes, the predictions of *Ec*HypCD were repeated with modified settings (see Methods) that allow more flexibility, and indeed complexes with open and closed conformations of the C-terminal part of HypC were predicted (**Fig. 5c**). Significantly, in all predictions, the structures of HypD and the β-barrel core domain of HypC remain virtually unchanged, while the major protein rearrangements are exclusively observed for the C-terminal part of HypC. Similar AlphaFold 2 predictions for *Tk*HypCD also resulted in different conformations for the C-terminal part (**Fig. 5d)**.

Strikingly, a primary docking site for ATP was calculated for *Ec*HypCD (Supplementary **Fig. S20**, Supplementary **Tables S7** and **S8**) that was almost identical (including the Vina score) to that of *Tk*HypCD (Supplementary **Fig. S21**, Supplementary **Tables S9** and **S10**). It is important to note, however, that ATP only docks in cavity A of *Ec*HypCD if the first three N-terminal amino acids Met-Cys-Ile of HypC (Met1 is cleaved by methionine aminopeptidase) were omitted from the docking calculations (Supplementary **Fig. S20**, Supplementary **Table S8**). These results are in line with the docking calculations performed on the experimentally determined coordinates of *Tk*HypCD (PDB: 3VYR), in which the position of Cys2 and Ile3 remained unresolved (**Fig. 3**, Supplementary **Table S5**). Consistently, docking calculations using an AlphaFold-predicted *Tk*HypCD complex, which contained the Cys2-Ile3 dipeptide, confirmed that ATP cannot dock to cavity A (Supplementary **Fig. S21,** Supplementary **Table S9**). Based on these observations, we hypothesized that both the C-terminal part of HypC must be in the open conformation and the outermost N-terminus of HypC must change its conformation to allow the binding of ATP in cavity A. In addition, the consistent AlphaFold 2 structure predictions and CB-Dock2 docking data for different HypCD scaffold complexes may allow conclusions to be drawn about HypC dynamics and its functioning. Since the structural changes are restricted to a small part of the HypCD protein complex, we searched for an experimental method to detect such (dynamic) conformational changes. In recent years, crosslinking mass spectrometry (crosslinking MS) has emerged as key technology in structural biology for investigating protein conformations and protein-protein interactions [39–42]. Holo- and apo-*Ec*HypCs-D preparations with or without ATP were treated with the UV-activatable crosslinker sulfo-SDA, which introduces specific distance constraints

into proteins with an upper limit (Cα-Cα) between 25-30 Å, for subsequent crosslinked residue pairs (using a 1% link-level false discovery rate). The crosslinked protein samples were subjected to trypsin digestion, and the resulting (crosslinked) peptide mixtures were then analyzed using MS as described in the Methods section.

The crosslinking MS data obtained for holo-HypCs-D (± ATP) are shown in **Fig. 6**. Significantly, we indeed observed crosslinks indicating the existence of both, an open and a closed conformation of the C-terminal part of HypC in the HypCs-D complex. The crosslinks supporting that the C-terminal part of HypC is positioned in the closed conformation in holo-HypCD (–ATP) include that of residue K98, belonging to the Strep-tag II sequence located at the C-terminus of HypC, with HypD residues Y363, Q368 and Y365 (**Fig. 6a**, blue area) with an estimated distance of 22.5, 21.6 and 19.2 Å, respectively, according to the corresponding AlphaFold 2 model (**Fig. 6b**, **Table 1**). In contrast, in the HypCs-D model, where HypC is in the open conformation (**Fig. 6c**), the estimated distances between the above-mentioned amino acid residues exceed the maximum expected length of 25-30 Å (**Table 1**) for chemical cross-linking [43]. Other diagnostic cross-links are those between K98 of HypCs and the HypD residues Y122, S123, A131, N134, P135 and T136 (**Fig. 6a**, yellow area). Here the distances span between 26 and 39 Å for the closed and between 62 and 86 Å for the open conformation (**Table 1**). Taking into account the flexibility of the Strep-tag II, which is not confidently predicted by AlphaFold 2 model (Supplementary **Fig. S19**), as well as the larger distances for K98 of HypCs and the residues of HypD in the open conformation that exceed the maximum distance for cross-links, the MS data support the closed conformation of the C-terminal part of HypCs in holo-HypCs-D (–ATP). Consistently, the above-mentioned crosslinks were not detected in the holo-HypCs-D incubated with ATP, suggesting that the binding of the nucleotide causes the observed (and predicted) conformational changes in HypCD (**Fig. 6a**). Moreover, the ATP-induced changes described above were not observed for apo-HypCs-D (Supplementary **Fig. S22**), implying that the closed conformation of the C-terminal part is only induced in the absence of ATP when the protein is loaded with the $Fe(CN)_2CO$ cofactor.

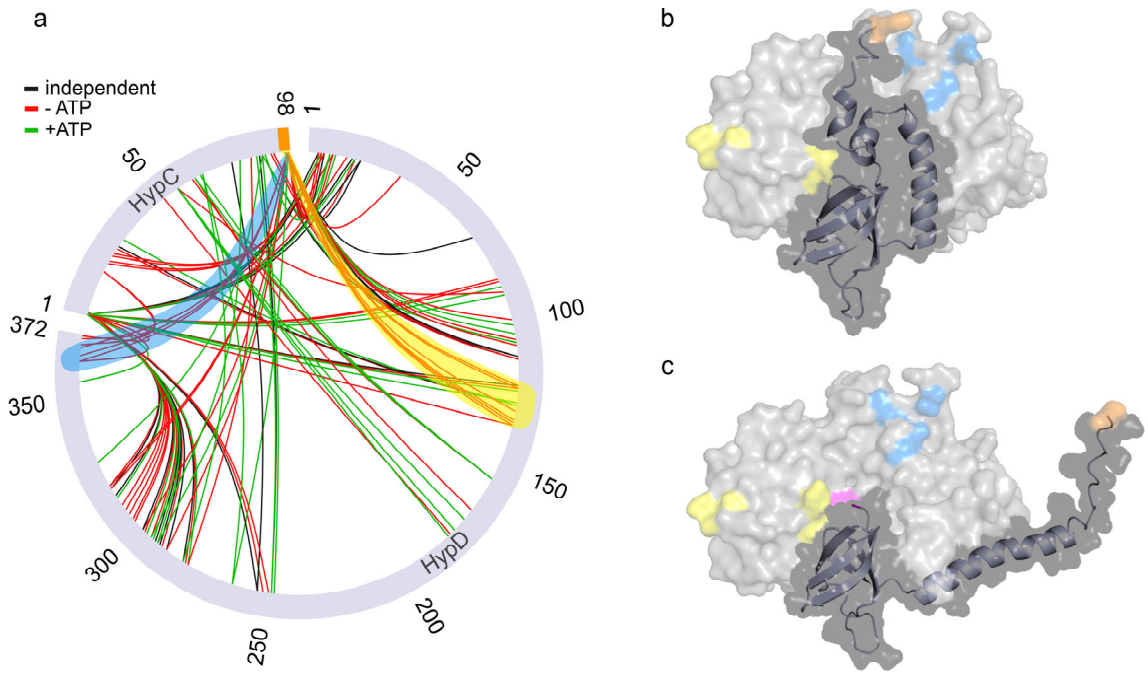

Fig. 6. Crosslinking MS analysis of holo-HypC$_S$-D with and without ATP. a Circular view of the mass spectrometry analysis of the crosslinking within the holo-*Ec*HypC$_S$-D complex with or without ATP. HypC and HypD sequences are represented as grey, scaled bars and labeled accordingly. Amino acid numbering is given on the outside of the circle. Crosslinks between the two proteins are depicted as red (–ATP) and green (+ATP) lines. Cross-links observed in both samples are depicted as black lines (independent). Cross-links that support a closed conformation of the C-terminal part of HypC (panel **b**) are highlighted in transparent yellow and blue. The yellow area includes the residues K98 to Y122 as well as S123, A131, N134, P135 and T 136 and the blue area includes the residues K98 to Y363 as well as Y365 and Q368. The distances between the amino acids of these crosslinks (aa to aa) were determined with PyMol and are listed in **Table 1**. Crosslinks in regions of the protein complex remote from the predicted ATP binding site are not discussed. Panels **b** and **c** show the AlphaFold 2-predicted *Ec*HypC-D structures in closed and open conformation, respectively, which contain the Strep-tag II peptide sequence at the C terminus of HypC. K98$_{HypC}$ is colored in orange and C2$_{HypC}$ in magenta. The colors of other highlighted residues correspond to color code used in panel **a**. Note that C2$_{HypC}$ in the closed conformation is covered by the C-terminal part of HypC and therefore not visible.

Table 1 | Amino acid distances of selected crosslinks in holo-HypCD that indicate an open or a closed conformation of the C-terminal part of HypC

Cross-link (aa - aa)[a]	Distance (in Å) for **closed** conformation	Distance (in Å) for **open** conformation
K98 - Y363	20.8	47.6
K98 - Y365	16.3	51.1
K98 – Q368	17.5	46.3
K98 – Y122	26.3	62.0
K98 – S123	29.5	64.3
K98 – A 131	35.8	79.4
K98 – N134	34.4	79.5
K98 – P135	39.3	84.0
K98 – T136	38.9	85.6

[a]Blue and yellow colors correspond to those in **Fig. 6**.

Our *in vitro* assays demonstrated that HypCD utilizes ATP to deliver the $Fe(CN)_2CO$ fragment to the apo-form of the hydrogenase large subunit. The combination of the AlphaFold 2 and crosslinking MS data indicate that this may occur through ATP-dependent conformational changes in HypCD, mainly at the C-terminal part of HypC, which suggests a competition-controlled mechanism of transfer for the $Fe(CN)_2CO$ fragment. As ATP and the $Fe(CN)_2CO$ fragment cannot bind simultaneously to the same protein pocket due to steric hindrance (both cofactors are predicted to be located at close distance from Cys38 in HypD), we propose that the binding of ATP triggers the dissociation of the $Fe(CN)_2CO$ fragment from Cys38 in HypD. Consequently, the $Fe(CN)_2CO$ synthon would remain bound to Cys2 of HypC. This scenario is consistent with a recent report by Gary Sawers´ group showing that the HybG maturase (a HypC paralog) dissociated from HypD carries the $Fe(CN)_2CO$ group, as evidenced by tandem MS/MS experiments [16]. HypC/HybG loaded with $Fe(CN)_2CO$ would then deliver the iron fragment to apo-form of the hydrogenase large subunit.

To structurally elucidate this interaction, we used AlphaFold 2 to compute a HypC-HoxC protein complex. The model predicts possible interactions between the two proteins, whereby Cys2 of HypC points towards the open cavity of the [NiFe]-binding site of HoxC (Supplementary **Fig. S23**). However, the low predicted aligned error (PAE) values for the HypC-HoxC complex (Supplementary **Fig. S19**) indicate that the model is not highly reliable for the relative position of the two proteins to each other and, consequently, also for the position of the N-terminus of HypC. By using the recently released AlphaFold 3 server, which allows structural predictions of protein complexes with nucleic acids, small molecules and even metal ions [44] a stable and highly reliable HypC-HoxC complex was predicted (**Fig. 7a** and Supplementary **Fig. S24** for PAE and pTM scores), in which the $Cys2_{HypC}$ protrudes into the [NiFe]-binding site of HoxC. Interestingly, the presence of an Fe ion in the active center (**Fig. 7b**), which mimics the assembled $Fe(CN)_2CO$ fragment, induces a displacement of Cys482 of HoxC, which now strikingly adopts an arrangement reminiscent of the structure of the apo-large subunit HyhL from *T. kodakarensis* in complex with the Ni-chaperone HypA [45]. Importantly, both the HypCD (Supplementary **Fig. S25**) and HypCDE (Supplementary **Fig. S26**) complexes show no significant interactions with the large hydrogenase subunit according to the corresponding AlphaFold 2 models, which strengthens the hypothesis that the HypC protein alone delivers the $Fe(CN)_2CO$ unit to the apo-form of the hydrogenase large subunit.

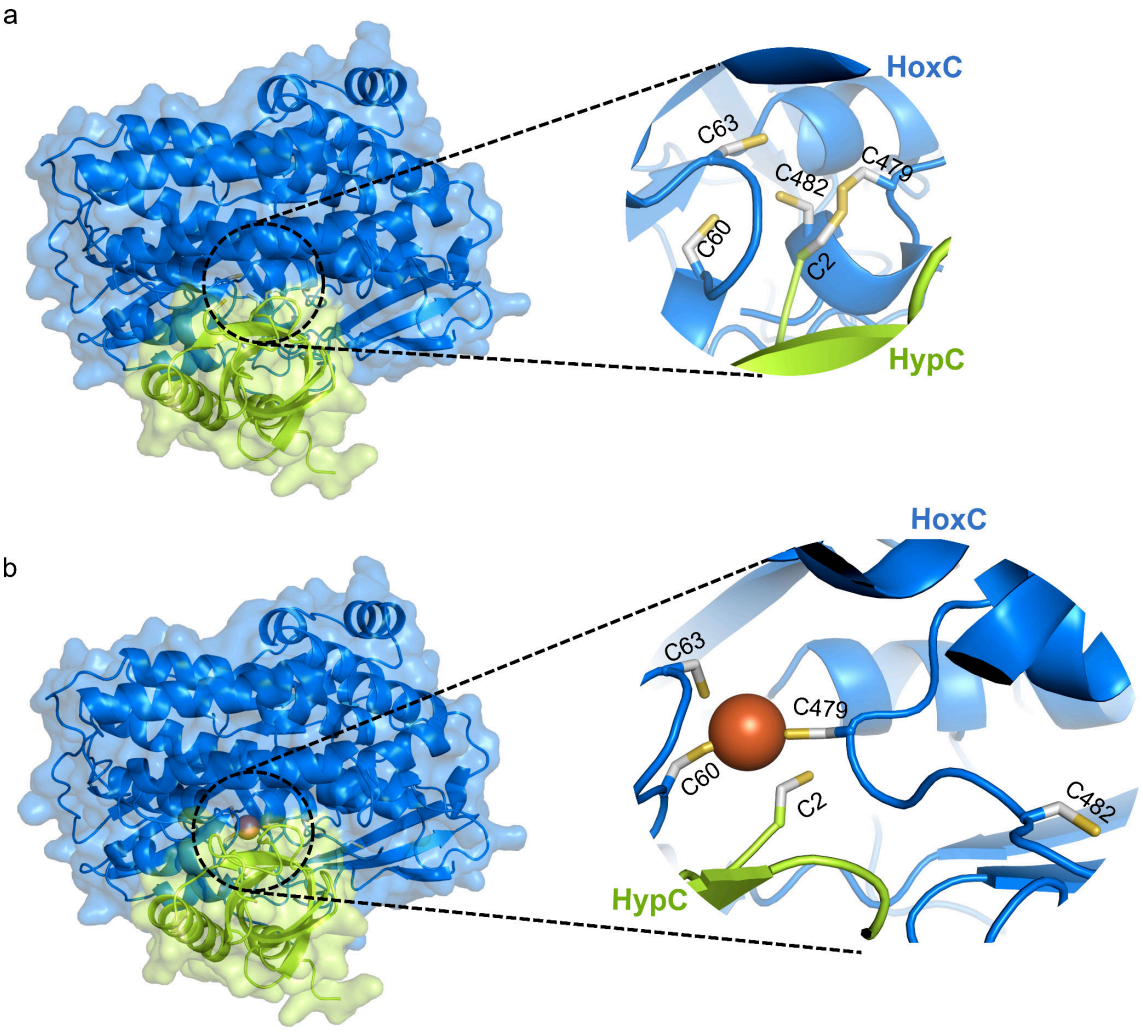

Fig. 7. AlphaFold 3-predicted complexes between *Ec*HypC and *Cn*HoxC. (**a**) Cys2 of HypC protrudes into the [NiFe]-binding motif of HoxC, comprising the residues Cys60, 63, 479 and 482. (**b**) The predicted HypC-HoxC complex calculated in the presence of an Fe ion exhibits structural changes involving Cys482 of HoxC, which undergoes large displacements as compared to the predicted model in **a**. Note that Cys2 of HypC is still close to the [NiFe]-binding site. HoxC (blue) and HypC (green) are shown in surface and cartoon representations, and the [NiFe]-binding site of HoxC is shown in ball and stick representation with S in yellow; C in grey and Fe in brown.

Discussion

In this study, we investigated a key step in the assembly of the [NiFe]-hydrogenase active site, which is the HypCD-mediated incorporation of the low spin $Fe^{II}(CN)_2CO$ synthon into the apo-hydrogenase large subunit. Based on our biochemical, spectroscopic and computational data, we draw the following conclusions about the role of the HypCD scaffold complex.

(1) Holo-HypCD houses two Fe-containing cofactors, a [4Fe–4S] cluster and a low-spin Fe^{II} species with a five-fold coordination comprising one CO, two CN^- and two cysteine thiolates ($Cys2_{HypC}$ and $Cys41_{HypD}$, *E. coli* numbering) as ligands. (2) Binding of ATP, not its

hydrolysis, is required for transfer of the $Fe(CN)_2CO$ moiety to the apo-form of the hydrogenase large subunit. Protein-ligand docking data identified an ATP binding site in a HypD cavity at the HypC-HypD interface. (3) The binding of ATP presumably takes place in the cavity that also accommodates the $Fe(CN)_2CO$ synthon, and, among others, the synthon-binding Cys41 of HypD is involved in the ATP binding. Considering that Cys2 of HypC and Cys41 of HypD must be close to each other to stably bind the $Fe(CN)_2CO$ fragment [32], we propose that the binding of ATP triggers significant rearrangements in HypCD, resulting in i) the disruption of the $Fe(CN)_2CO$ thiolate complex with Cys41 of HypD and ii) the displacement of the N-terminal Cys2 of HypC, which alone carries the $Fe(CN)_2CO$ fragment. As this step requires reducing power, the [4Fe–4S] cluster and the nearby thioredoxin (dithiol–disulfide) moiety represent possible electron donors [22]. (4) AlphaFold 2 structure predictions and cross-linking mass spectrometry revealed significant ATP-dependent conformational changes of the C-terminal, mostly α-helical part of HypC exclusively in the holo-HypCD complex. An open and a close conformation were identified that could reliably regulate the binding/dissociation of the ATP/$Fe(CN)_2CO$ cofactors, as depicted in **Fig. 8**. (5) It has been hypothesized that the HypCD complex dissociates to allow the delivery of the $Fe(CN)_2CO$ fragment to apo-form of the hydrogenase large subunit[16]. Our AlphaFold 3 data allow us to visualize a possible Fe-dependent interaction between the N-terminus of HypC and the [NiFe]-binding site of the large subunit HoxC.

In summary, our results provide new insights into the sophisticated protein machinery responsible for [NiFe]-hydrogenase maturation. Although the importance of NTPases for the assembly of metallocofactors is widely recognized [46], and the ATP-dependent [NiFe]-hydrogenase maturases HypE and HypF are good examples[6] , the role of ATP hydrolysis by HypCD[17,18] remains enigmatic. In terms of structure, function and NTPase activity, there are, however, interesting similarities between HypCD and the [FeFe]-hydrogenase maturase HydF, which carries a [4Fe–4S] cluster and has a low GTPase activity whose role in maturation is unknown like the ATPase activity of HypCD [47–49]. Considering that apo-HypCD also exhibits ATPase activity and that ATP has recently been shown to stabilize iron (Fe^{II}-ATP complex) in the labile iron pool of the cytoplasm of *E. coli*[50], ATP (hydrolysis) might play a role at an earlier stage in the maturation of [NiFe]-hydrogenases. For example, ATP might deliver an Fe ion to apo-HypCD and thus support the assembly of Fe precursor fragments and/or enable the interaction of HypCD with other maturases. Future work will address these open questions.

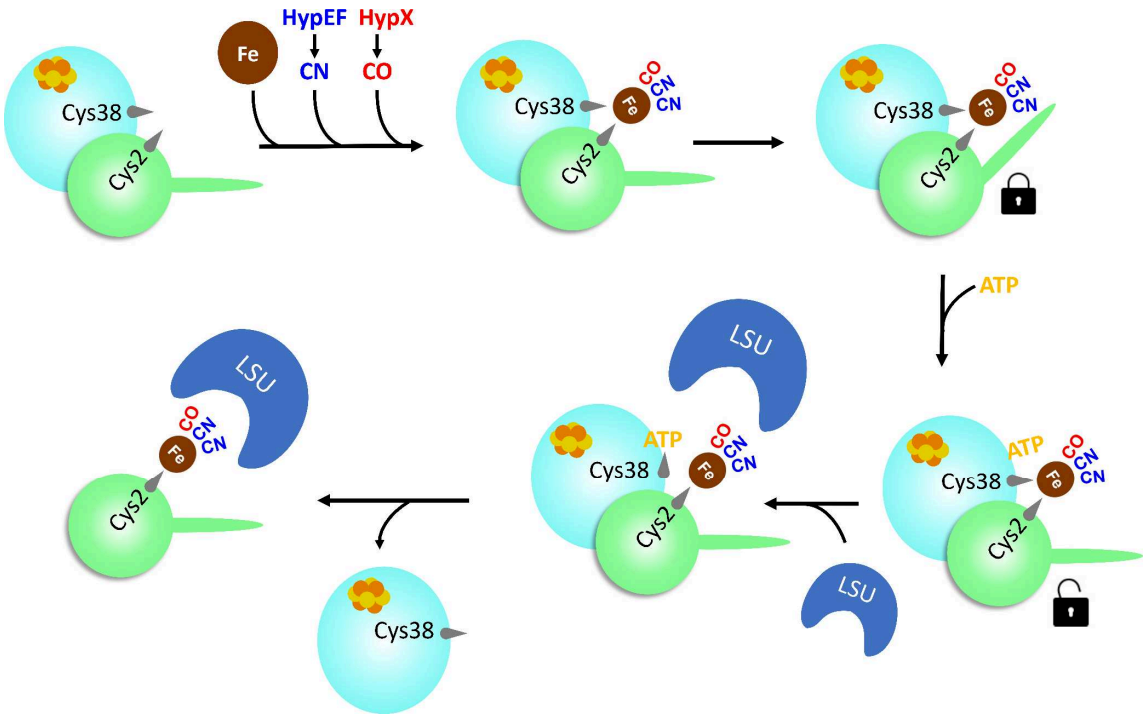

Fig. 8. Scheme for the transfer of the $Fe(CN)_2CO$ fragment from HypCD to the apo-form of the hydrogenase large subunit. The [4Fe–4S]-cluster containing HypD protein is depicted in cyan and HypC in green. The C-terminal part of HypC remains in the open conformation until the $Fe(CN)_2CO$ synthon coordinated by $Cys38_{HypD}$ and $Cys2_{HypC}$ is fully assembled. Our data indicate that the C-terminal part of HypC in holo-HypCD adopts the closed conformation that protects the $Fe(CN)_2CO$ fragment until further use. Subsequent ATP binding firstly causes the HypC protein to adopt the open conformation and secondly, presumably in the presence of the large subunit (LSU), leads to the disruption of the $Fe(CN)_2CO$–S bond with Cys38 of HypD and the concomitant rearrangement of the N-terminal Cys2 of HypC with the bound $Fe(CN)_2CO$ fragment. These structural changes are thought to destabilize the HypCD complex, thereby releasing the $Fe(CN)_2CO$-loaded HypC, which is then proposed to form a transient complex with LSU to deliver the $Fe(CN)_2CO$ fragment (**Fig. 7**).

Methods

Bacterial strains, cultivation conditions and protein purification

For heterologous protein production, *E. coli* strain Rosetta (DE3) was used. The corresponding expression plasmids are listed in Supplementary **Table S2** and their construction is described in Supplementary Methods (Supplementary **Table S11)**. Strains were grown aerobically in LB medium containing 100 µg/mL carbenicillin and 34 µg/mL chloramphenicol. Precultures were grown overnight at 37 °C and used to inoculate (1:100) 1-L main cultures, which were subsequently cultivated at 37 °C and 120 rpm until an OD_{600} between 0.4-0.8 was achieved. Gene expression was induced by adding 0.5 mM isopropyl beta-D-1-thiogalactopyranoside (IPTG). The cells were incubated overnight at 16 °C and 120 rpm and finally harvested by centrifugation at 11,500 x *g* for 15 min at 4 °C. Cell pellets were either processed immediately

or frozen in liquid nitrogen and stored at -80 °C. All purification steps were performed aerobically at 4 °C. 1 g of cell pellet was resuspended in 3 mL of the corresponding buffer (Supplementary **Table S1**). Cell lysis was achieved in a French pressure cell with a pressure of 125 MPa. After ultracentrifugation at 100,000 x *g* for 45 min at 4 °C, the soluble extract was loaded onto either a Strep-Tactin Superflow® resin (high-capacity, IBA Lifesciences) column or a HisPur® Ni-NTA resin (Thermo Scientific) column, depending on the affinity tag. The washing, elution procedures as well as the buffer compositions are listed in Supplementary **Table S1**. Eluted proteins were first concentrated (Ultracel® Amicon® Ultra 15 mL centrifugal filter units), followed by a 10-fold dilution with washing buffer and then concentrated again by ultrafiltration. This process was repeated four times to wash away residual imidazole or D-desthiobiotin. Finally, protein aliquots were frozen and stored in liquid nitrogen. Concentration was determined via the Pierce BCA protein assay kit (Thermo Scientific).

Production of ^{57}Fe-labeled HypCD proteins was conducted as follows. When HypCD-overproducing cell cultures reached an OD_{600} between 0.4-0.8, 2.5 mL of $^{57}FeCl_2$ solution (20.5 mM in 1.5 M HCl) were added to achieve a final concentration of ca. 50 µM. Cells were first incubated for ~20 min at room temperature (RT) and gene expression was then induced as described above. All purification steps were identical to those used to isolate HypCD from media containing iron with natural isotope distribution.

Polyacrylamide gel electrophoresis and metal determination

Protein purity was verified by SDS-PAGE. 3.5 µg of purified proteins were separated on a 15% acrylamide separating gel at 0.04 A for ca. 45 min. Protein bands were visualized by Coomassie staining. The metal content of purified HypCD samples was determined via inductively coupled plasma optical emission spectrometry (ICP-OES). Three technical replicates of a 10 µM protein solution (each 500 µl) were mixed with 500 µl nitric acid (65 % v/v). After being incinerated at 100 °C overnight, samples were filled up to 5 mL with ultrapure water and measured in an Optima 2100DV ICP-OES (Perkin-Elmer). The same procedure was repeated for three technical replicates of the buffer solution.

ATPase activity of HypCD

ATPase activity was determined biochemically using a coupled enzymatic assay comprising a pyruvate kinase (PK) and a lactate dehydrogenase (LDH) from rabbit muscle (Sigma) [51]. In a first reaction ATP is hydrolyzed by HypCD to ADP and phosphate. The produced ADP and phosphoenolpyruvate (PEP) are then used by PK to form pyruvate and ATP. Last, pyruvate is consumed by LDH to form lactate. During this last assay reaction, NADH is oxidized to NAD^+, which is detected by UV-Vis spectroscopy due to the decrease in absorbance at 340 nm

($\varepsilon = 6.3\ mM^{-1}\ cm^{-1}$)[52]. Each reaction was conducted at 25 °C in buffer containing 100 mM Tris/HCl, pH 7.5, 2.5 mM $MgCl_2$, 1 mM PEP, 1 mM ATP and 0.3 mM NADH. The final amount of PK and LDH was 4 U and 3 U, respectively. To avoid an unspecific increase of absorbance due to residual ADP in the reaction mixture, HypCD was added when the absorbance of the solution reached a plateau. To verify that HypCD was exclusively responsible for ATP hydrolysis, we also recorded IR spectra of ATP with and without HypCD by monitoring the absorbances of the reactant and the hydrolysis products (Supplementary **Fig. S13**). In this case, HypCD was incubated in an anaerobic workstation with ATP, NaDT and $MgCl_2$ in a molar excess of 40-fold, 30-fold and 20-fold, respectively, and the mixture then transferred to the IR cell.

Spectroscopy

Infrared

HypCD and HoxC protein solutions were transferred into a homemade, gas-tight, and temperature-controlled (10 °C) transmission cell equipped with two sandwiched CaF_2 windows separated by a Teflon spacer (optical pathlength of 50 µm). Spectra with a resolution of 2 cm^{-1} were recorded using a Bruker Tensor 27 Fourier-Transform spectrometer equipped with a liquid nitrogen-cooled mercury-cadmium-telluride detector. The sample compartment was purged with dried air. For a single spectrum 200 individual scans were averaged. A buffer spectrum was used as reference to calculate the corresponding absorbance spectra. Bruker OPUS software version 7.5 was used for data analysis.

Mössbauer

Zero-field Mössbauer spectra of ^{57}Fe-labeled HypCD apo- and holo-samples at a concentration of ca 1.5 mM were acquired on a SEECO MS6 spectrometer comprising the following instruments: a JANIS CCS-850 cryostat, including a CTI-CRYOGENICS closed cycle 10 K refrigerator, and a CTI-CRYOGENICS 8200 helium compressor. The cold head and sample mount were equipped with calibrated DT-670-Cu-1.4L silicon diode temperature probes and heaters. The temperature was controlled by a LAKESHORE 335 temperature controller. Spectra were recorded using an LND-45431 Kr gas proportional counter with beryllium window connected to the SEECO W204 γ-ray spectrometer that includes a high voltage supply, a 10 bit and 5 µs ADC and two single channel analyzers. Motor control and recording of spectra were taken care of by the W304 resonant γ-ray spectrometer. For the reported spectra a RIVERTEC MCO7.114 source (^{57}Co in Rh matrix) with an activity of about 1 GBq was used. All spectra were recorded on frozen solutions at 13 K, and data were accumulated for about 24-

72 hours. Mössbauer data were processed and simulated using the WMOSS4 program (www.wmoss.org). Isomeric shifts are referenced to α-iron at room temperature.

NRVS

NRVS measurements were conducted at Petra III P01 (Germany) using 14.41 keV radiation (^{57}Fe). Raw NRVS data were converted to single-phonon ^{57}Fe partial vibrational densities of states (PVDOS) using the PHOENIX software package via the "NRVS Spectra Processing Tool" web interface (https://www.spectra.tools/). The energy scales were calibrated with a [NEt_4][$^{57}FeCl_4$] sample characterized by two prominent peaks at 378 cm^{-1} (asymmetric Fe–Cl stretching mode), and 139 cm^{-1} (Fe–Cl bending mode) [53]. The temperature of the samples was maintained at ca. 12 K using a liquid He cryostat. The real sample temperature, as obtained from the spectral analysis, was 40-50 K. To enhance the signal/noise ratio in the Fe–CO/CN spectral range, sectional measurements were performed. Each scan was divided into two segments with different data collection times (second per point, s/pt). We used 3-4 s/pt for the region from –80 to 360 cm^{-1} and 9-10 s/pt for the region from 360 to 700 cm^{-1}.

UV-Visible

UV-vis spectra were recorded using a Cary®50 UV-Vis spectrophotometer (Varian, Agilent, USA) at room temperature. Each protein was used with a concentration of 40 µM. A buffer spectrum was used as a reference.

Cross-linking mass spectrometry

Apo-HypCs-D was purified by affinity chromatography, while holo-HypCs-D was additionally subjected to size-exclusion chromatography on a Superdex 200 Increase 10/300 GL (Cytiva) to remove unwanted oligomers (ternary HypCDE complex, HypC dimers). Purified HypCD complex (20 µg, 0.5 mg/mL) was crosslinked using sulfo-SDA (sulfosuccinimidyl 4,4'-azipentanoate (Thermo Scientific Pierce) at 0.76 mM in a crosslinking buffer (MOPS 50 mM, 150 mM NaCl, 0.1 mM DTT, pH 7.5). For the HypCD plus ATP sample, ATP was added to purified HypCD (9 mM final crosslinking reaction concentration) 10 min prior to addition of crosslinker. The crosslinking reaction involved two steps: 1. Crosslinker and protein were incubated for 30 minutes at room temperature in the dark; 2. the sample was irradiated with high-power UV light (LuxiGen™ 365 nm UV LED Gen 4 Emitter, LED Engine, operated at 1000 mA) for 20 seconds. After crosslinking, protein was acetone-precipitated and digested using an adapted SPEED protocol [54]. Briefly, pelleted proteins were dissolved in 10 µL trifluoracetic acid (TFA), neutralized by addition of 100 µL 2M TrisBase, and reduced and alkylated with the addition of 11 µL TCEP/2-chloroacetamide (at final concentrations of 10 mM and 40 mM, respectively) and heating for 5 mins at 95 °C. Protein samples were diluted

1:5 with water and digestion was carried out for 20 h at 37 °C using trypsin at an enzyme:protein ratio of 1:50. Digests were acidified with TFA and desalted using C18 StageTips [55].

LC-MS/MS analysis was performed on a Q Exactive High-Field (HF) Hybrid mass spectrometer (Thermo Fisher Scientific) coupled to an Ultimate 3000 UHPLC system (Dionex, Thermo Fisher Scientific). Peptides were separated on a 50 cm EASY-Spray column (Thermo Fisher). Mobile phase A consisted of 0.1% (v/v) formic acid and mobile phase B of 80% (v/v) acetonitrile with 0.1% (v/v) formic acid. The following LC gradient was applied with a flowrate of 300 nL/min: 2% B to 11% B in 10 min, to 35% B in 77 min, to 50% B in 5.5 min, ramping to 95% B in 2.5 min and holding for 5 min (total run time, 120 min). Mass spec data were acquired in data-dependent mode, with both MS1 and MS2 scans carried out in the Orbitrap. Full scan mass spectra were recorded in the range of 400-1450 m/z at a resolution of 120,000 (AGC target, 1e6; injection time of 50 ms). The ten most intense ions in the full scan, with precursor charge states between 3+ and 6+, were isolated with a m/z window of 1.4 Th and fragmented using higher-energy collision-induced dissociation (HCD) at stepped normalized collision energies of 20, 28 and 30%. Subsequent fragmentation spectra were recorded at a resolution of 60,000, using an AGC target of 2e5 and maximum injection time set to 250 ms. Dynamic exclusion (single repeat count) was set to 30 s. Precursors m/z were recalibrated based on linear peptide identifications at <1% False Discovery Rate (FDR). Recalibrated peak lists were searched for crosslink identification against the sequences of HypC and HypD, using the Xi software suite (version 1.7.6.4; https://github.com/Rappsilber-Laboratory/xiSEARCH) [56] with the following settings: MS1 accuracy, 3 ppm; MS2 accuracy, 5 ppm; enzyme, trypsin, allowing up to 2 missed cleavages and 2 missing monoisotopic peaks; crosslinker, SDA (NHS-ester reaction specificity for lysine, serine, threonine, tyrosine and protein N-termini); fixed modifications, carbamidomethylation on cysteine (cm, +57.02 Da); variable modifications, methylation on glutamic acid (me, +14.01), oxidation on methionine (ox, +15.99 Da), SDA-loop (+82.04 Da) and SDA-hyd (+100.05). SDA MS-cleavability was considered during database search. Identified crosslinks were filtered to 1% FDR on link level with xiFDR version 2.2.RC2 [42].

3D structure predictions

The AlphaFold 2 models of HypCD complexes from *Thermococcus kodakarensis* (*Tk*) and *Escherichia coli* (*Ec*), the latter with and without the Strep-tag II sequence at the C terminus of HypC, as well as the complex between *Ec*HypC and HoxC from *C. necator* (*Cn*) were calculated using ColabFold v1.5.5 [57,58]. For prediction of conformational variability, the following settings were applied: “max_msa” was set to “32:64”, “num_seeds” was set to “16”,

and "use_dropouts" was not activated ("use_dropouts" did not lead to obvious structural changes when activated) [59]. The accession numbers of the protein sequences used for the AlphaFold structure predictions (Supplementary **Data I**) are listed in **Table 2**. During preparation of the manuscript, AlphaFold 3 was released [44] and we used it to compute both the HypCD and HypC-HoxC complexes in the presence of ATP and Fe ions. The interatomic distances listed in **Table 1** were determined using PyMOL 2.5.5 [60].

Table 2 Accession numbers of protein sequences used for AlphaFold structure predictions.

Protein[a]	**Accession number**
*Tk*HypCD	3vyr (RCSB)
*Ec*HypC	P0AAM3 (UniProt)
*Ec*HypD	P24192 (UniProt)
*Ec*HybG	P0AAM7 (UniProt)
*Cn*HoxC	Q79IP6 (UniProt)

[a] *Tk - Thermococcus kodakarensis, Ec - Escherichia coli, Cn - Cupriavidus necator.*

DFT calculations

DFT Model Setup. Initial coordinates used for the density functional theory (DFT) modeling were constructed based on the (*i*) cofactor-free AlphaFold prediction of the *Ec*HypCD protein structure, and (*ii*) $Fe(CN)_2(CO)(Cys)_2$ fragment extracted from the PDB 3RGW [61] (X-ray structure of the O_2-tolerant membrane-bound [NiFe]-hydrogenase from *Cupriavidus necator*). The $Fe(CN)_2(CO)(Cys)_2$ fragment was docked manually into the *Ec*HypCD framework so that one of its cysteine side chains aligns with $Cys41_{HypD}$, and the second cysteine is positioned in the region of $Cys2_{HypC}$. Twelve more *Ec*HypCD residues in the environment of $Fe(CN)_2CO$ were retained in the DFT model as shown in **Fig. 2a** and Supplementary **Fig. S6**, overall defining the system as $[\mathbf{C_2}]_{HypC}$ – $Fe(CN)_2(CO)$ – $[\mathbf{C_{41}}G_{42}G_{43}H_{44}$ / $G_{68}C_{69}$* / F_{147} / T_{149} / $P_{199}G_{200}H_{201}$ / F_{227} / $E_{357}]_{HypD}$ (metal ligands are in bold). Here, the backbone spacers were included between the consecutive HypD residues. The side chain of $Cys69_{HypD}$ (*) was omitted, equivalent to a C-to-G modification, as it points away from the cofactor. All the C_α carbon atoms were fixed to their reference AlphaFold positions during DFT structure optimization (see method details below) as often employed in protein modeling [62], except that of $Cys2_{HypC}$, which varies its position (see the Results section). The titratable imidazole groups of $His44/201_{HypD}$ were singly protonated corresponding to the neutral pH. In contrast, $Glu357_{HypD}$ carboxylate was protonated due to its proximity to the $Cys2_{HypC}$ thiolate sulfur (**Fig. 2a** and Supplementary **Fig. S6**).

DFT Methods. Molecular geometry optimization and subsequent Hessian were accomplished using GAUSSIAN 16 Revision C.01 [63], assisted with densities exported from single-point calculations using JAGUAR 11.0 [64]. All calculations employed PBE0 [65] hybrid functional, and LACV3P** basis set as implemented in JAGUAR. For the 1st- and 2nd-row elements, LACV3P** implies 6-311G** triple-ζ basis sets including polarization functions. For the Fe center, LACV3P** consists of a triple-ζ basis set for the outermost core and valence orbitals, and the quasi-relativistic Los Alamos effective core potential (ECP) for the innermost electrons [66,67]. Molecular environment was considered using a self-consistent reaction field (SCRF) polarizable continuum model and integral equation formalism[68] (IEF-PCM) as implemented in GAUSSIAN. The static dielectric constant was set to $\varepsilon = 4.0$, as often used for proteins, and the remaining IEF-PCM parameters were kept at their default values for water. The ^{57}Fe-PVDOS and interatomic relative displacement kinetic energy distribution (KED) intensities were extracted from GAUSSIAN normal mode outputs using an in-house program Q-SPECTOR [69]. To empirically account for the observed NRVS lineshape, the computed ^{57}Fe-PVDOS intensities were broadened by Lorentzian convolution with a full width at half maximum (FWHM) = 14 cm^{-1}. For ^{57}Fe-PVDOS, empirical scaling by ×1.07/1.02/0.97 was applied to the calculated frequencies in the 400-560/560-610/610-660 cm^{-1} regions, respectively.

In vitro transfer assay

All steps were carried out under anaerobic conditions in an anaerobic workstation with a temperature of ca. 10 °C. Buffer solutions and protein concentrators (Amicon Ultracel, Millipore, 30 kDa cutoff) were degassed prior usage and equilibrated with anaerobic buffer. The assay was carried out in a 1.5 mL Eppendorf vial with the following components: 50 mM MOPS/KOH, pH 7.4 at 4°C, 150 mM NaCl, 15 mM NaDT, 10 mM $MgCl_2$, 20 mM of ATP/GTP/non-hydrolysable ATP analogue (see Supplementary **Table S6** for further details). 0.06 mM apo-HoxC$_S$ was reacted with 0.3 mM holo-HypC$_H$-D protein solution (5 molar equivalents). After incubation, the whole assay reaction was loaded on a Strep-Tactin Superflow® column (high-capacity, iba Lifescience) with a column volume (CV) of 1 mL, to isolate HoxC$_{strep}$ from the reaction mixture. The column was washed with 10 CVs of washing buffer (50 mM MOPS/KOH, pH 7.4 at 4°C, 150 mM NaCl) and the matrix-bound protein was eluted with 5 CVs of washing buffer supplemented with 3.0 mM d-desthiobiotin. Elution fractions were concentrated using Ultracel® Amicon® Ultra 0.5 mL centrifugal filter units (cutoff 30 kDa) followed by a 5-fold dilution step with washing buffer to remove residual desthiobiotin. The washing step was repeated 4 times, followed by a final step of protein concentration (resulting volume of ca. 20 µL) and IR measurements.

CB-Dock2 cavity detection-guided blind docking

For a protein-ligand blind docking simulation the online tool CB-Dock2 was used [34,35]. The X-rays coordinates of *T. kodakarensis* HypCD [32] and the AlphaFold-predicted structures of *E. coli* HypCD (Supplementary **Data I**) were employed as proteins. As ligand, the coordinates of ATP (DrugBank ID: DB00171) were used. The docking simulation is based on a perl script that processes the submitted files as described at https://cadd.labshare.cn/cb-dock2/php/manual.php. AutoDock-Vina (version 1.2.0) is used for template-independent blind docking and template-based blind docking uses BioLip database (version 2021.09.15) as the template database. Output files are given as receptor-ligand PDB files for all detected cavities (Supplementary **Data II**).

Acknowledgments

This work was supported by the Deutsche Forschungsgemeinschaft (DFG, German Research Foundation) through the SPP 1927 'Iron Sulfur for Life' project no 311062227 (O.L., I.Z., A.K.), project 449713269 (A.B.) and the cluster of excellence 'UniSysCat' under Germany's Excellence Strategy-EXC2008-390540038. G.C., V.P., M.A.M., and O.L. thank the COST Action FeSImmChemNet, CA21115, supported by COST (European Cooperation in Science and Technology). The Wellcome Centre for Cell Biology is supported by core funding from the Wellcome Trust [203149] (J.R.). We acknowledge DESY (Hamburg, Germany), a member of the Helmholtz Association HGF, for the provision of experimental facilities. Parts of this research were carried out at Petra III. Beamtime was allocated for proposals I-20220851 and I-20210325. We thank Silke Leimkühler and coworkers (Universität Potsdam) for ICP-OES measurements.

Author contributions

A.K., G.C., A.C.S, and O.L. conceived and designed experiments,

A.K., G.C. and A.C.S. conducted molecular biology experiments;

A.K. and G.C. performed sample preparations and biochemical assays;

G.C. and A.K. performed sample preparation for synchrotron measurements;

G.C., A.K. and I.Z. performed and analyzed IR spectroscopic experiments;

K.W., G.C. and C.L. performed and analyzed Mössbauer experiments;

A.B., A.K. and J.R., performed and analyzed crosslinking mass spectrometry experiments.

G.C. and I.S. acquired and analyzed NRVS data;

V.P. and M.A.M. performed DFT modeling and analyzed the data;

A.K., G.C., and S.F. performed docking calculations, protein structure predictions and analyzed the data;

A.K., G.C., S.F., and O.L. wrote the manuscript with input from all co-authors.

All authors have given approval to the final version of the manuscript

Competing interests

The authors declare no competing interests.

References

1. Lubitz, W., Ogata, H., Rüdiger, O. & Reijerse, E. Hydrogenases. *Chem. Rev.* **114,** 4081–4148; 10.1021/cr4005814 (2014).

2. Jones, A. K., Lenz, O., Strack, A., Buhrke, T. & Friedrich, B. NiFe hydrogenase active site biosynthesis: identification of Hyp protein complexes in *Ralstonia eutropha*. *Biochemistry* **43,** 13467–13477; 10.1021/bi048837k (2004).

3. Böck, A., King, P. W., Blokesch, M. & Posewitz, M. C. Maturation of hydrogenases. *Adv. Microb. Physiol.* **51,** 1–71; 10.1016/s0065-2911(06)51001-x (2006).

4. Lacasse, M. J. & Zamble, D. B. NiFe-hydrogenase maturation. *Biochemistry* **55,** 1689–1701; 10.1021/acs.biochem.5b01328 (2016).

5. Watanabe, S., Sasaki, D., Tominaga, T. & Miki, K. Structural basis of NiFe hydrogenase maturation by Hyp proteins. *Biol. Chem.* **393,** 1089–1100; 10.1515/hsz-2012-0197 (2012).

6. Reissmann, S. *et al.* Taming of a poison: biosynthesis of the NiFe-hydrogenase cyanide ligands. *Science (New York, N.Y.)* **299,** 1067–1070; 10.1126/science.1080972 (2003).

7. Bürstel, I. *et al.* CO synthesized from the central one-carbon pool as source for the iron carbonyl in O_2-tolerant [NiFe]-hydrogenase. *Proc. Natl. Acad. Sci. U. S. A.* **113,** 14722–14726; 10.1073/pnas.1614656113 (2016).

8. Schulz, A.-C. *et al.* Formyltetrahydrofolate decarbonylase synthesizes the active site CO ligand of O_2-tolerant [NiFe] hydrogenase. *J. Am. Chem. Soc.* **142,** 1457–1464; 10.1021/jacs.9b11506 (2020).

9. Bürstel, I. *et al.* Probing the origin of the metabolic precursor of the CO ligand in the catalytic center of [NiFe] hydrogenase. *J: Biol. Chem.* **286,** 44937–44944; 10.1074/jbc.M111.309351 (2011).

10. Soboh, B. *et al.* The [NiFe]-hydrogenase accessory chaperones HypC and HybG of *Escherichia coli* are iron- and carbon dioxide-binding proteins. *FEBS Lett.* **587,** 2512–2516; 10.1016/j.febslet.2013.06.055 (2013).

11. Lacasse, M. J., Douglas, C. D. & Zamble, D. B. Mechanism of selective nickel transfer from HypB to HypA, *Escherichia coli* [NiFe]-Hydrogenase accessory proteins. *Biochemistry* **55,** 6821–6831; 10.1021/acs.biochem.6b00706 (2016).

12. Pinske, C., Thomas, C., Nutschan, K. & Sawers, R. G. Delimiting the function of the C-terminal extension of the *Escherichia coli* [NiFe]-hydrogenase 2 large subunit precursor. *Front. Microbiol.* **10,** 2223; 10.3389/fmicb.2019.02223 (2019).

13. Senger, M., Stripp, S. T. & Soboh, B. Proteolytic cleavage orchestrates cofactor insertion and protein assembly in [NiFe]-hydrogenase biosynthesis. *J. Biol. Chem.* **292,** 11670–11681; 10.1074/jbc.M117.788125 (2017).

14. Hartmann, S., Frielingsdorf, S., Caserta, G. & Lenz, O. A membrane-bound NiFe-hydrogenase large subunit precursor whose C-terminal extension is not essential for cofactor incorporation but guarantees optimal maturation. *MicrobiologyOpen* **9,** 1197–1206; 10.1002/mbo3.1029 (2020).

15. Caserta, G. *et al.* Stepwise assembly of the active site of [NiFe]-hydrogenase. *Nat. Chem. Biol.* **19,** 498–506; 10.1038/s41589-022-01226-w (2023).

16. Arlt, C. *et al.* Native mass spectrometry identifies the HybG chaperone as carrier of the $Fe(CN)_2CO$ group during maturation of *E. coli* [NiFe]-hydrogenase 2. *Sci. Rep.* **11,** 24362; 10.1038/s41598-021-03900-w (2021).

17. Nutschan, K., Golbik, R. P. & Sawers, R. G. The iron-sulfur-containing HypC-HypD scaffold complex of the [NiFe]-hydrogenase maturation machinery is an ATPase. *FEBS Open Bio.* **9,** 2072–2079; 10.1002/2211-5463.12743 (2019).

18. Haase, A. & Sawers, R. G. A redox-active HybG-HypD scaffold complex is required for optimal ATPase activity during NiFe-hydrogenase maturation in Escherichia coli. *FEBS Open Bio.* **13,** 341–351; 10.1002/2211-5463.13546 (2023).

19. Blokesch, M. *et al.* The complex between hydrogenase-maturation proteins HypC and HypD is an intermediate in the supply of cyanide to the active site iron of [NiFe]-hydrogenases. *J. Mol. Biol.* **344,** 155–167; 10.1016/j.jmb.2004.09.040 (2004).

20. Bürstel, I. *et al.* A universal scaffold for synthesis of the $Fe(CN)_2(CO)$ moiety of [NiFe] hydrogenase. *J. Biol. Chem.* **287,** 38845–38853; 10.1074/jbc.M112.376947 (2012).

21. Soboh, B. *et al.* [NiFe]-hydrogenase maturation: isolation of a HypC-HypD complex carrying diatomic CO and CN^- ligands. *FEBS Lett.* **586,** 3882–3887; 10.1016/j.febslet.2012.09.019 (2012).

22. Stripp, S. T. *et al.* Electron inventory of the iron-sulfur scaffold complex HypCD essential in [NiFe]-hydrogenase cofactor assembly. *Biochem. J.* **478,** 3281–3295; 10.1042/BCJ20210224 (2021).

23. Haase, A., Arlt, C., Sinz, A. & Sawers, R. G. Evidence the Isc iron-sulfur cluster biogenesis machinery is the source of iron for [NiFe]-cofactor biosynthesis in *Escherichia coli*. *Sci. Rep.* **14,** 3026; 10.1038/s41598-024-53745-2 (2024).

24. Pandelia, M.-E., Lanz, N. D., Booker, S. J. & Krebs, C. Mössbauer spectroscopy of Fe/S proteins. *Biochim. Biophys Acta* **1853,** 1395–1405; 10.1016/j.bbamcr.2014.12.005 (2015).

25. Roncaroli, F. *et al.* Cofactor composition and function of a H_2-sensing regulatory hydrogenase as revealed by Mössbauer and EPR spectroscopy. *Chem. Sci.* **6,** 4495–4507; 10.1039/c5sc01560j (2015).

26. Kamali, S. *et al.* Observation of the Fe-CN and Fe-CO vibrations in the active site of [NiFe] hydrogenase by nuclear resonance vibrational spectroscopy. *Angew. Chem. Int. Ed.* **52,** 724–728; 10.1002/anie.201204616 (2013).

27. Caserta, G. *et al.* In vitro assembly as a tool to investigate catalytic intermediates of [NiFe]-hydrogenase. *ACS Catal.* **10,** 13890–13894; 10.1021/acscatal.0c04079 (2020).

28. Ogata, H. *et al.* Hydride bridge in [NiFe]-hydrogenase observed by nuclear resonance vibrational spectroscopy. *Nat. Commun.* **6,** 7890; 10.1038/ncomms8890 (2015).

29. Caserta, G. *et al.* Hydroxy-bridged resting states of a [NiFe]-hydrogenase unraveled by cryogenic vibrational spectroscopy and DFT computations. *Chem. Sci.* **12,** 2189–2197; 10.1039/d0sc05022a (2020).

30. Lauterbach, L. *et al.* Characterization of the [3Fe-4S]$^{(0/1+)}$ cluster from the D14C variant of *Pyrococcus furiosus* ferredoxin via combined NRVS and DFT analyses. *Dalton Trans.* **45,** 7215–7219; 10.1039/c5dt04760a (2016).

31. Albareda, M., Palacios, J.-M., Imperial, J. & Pacios, L. F. Computational study of the $Fe(CN)_2CO$ cofactor and its binding to HypC protein. *J. Phys. Chem. B.* **117,** 13523–13533; 10.1021/jp407574n (2013).

32. Watanabe, S., Matsumi, R., Atomi, H., Imanaka, T. & Miki, K. Crystal structures of the HypCD complex and the HypCDE ternary complex: transient intermediate complexes during [NiFe] hydrogenase maturation. *Structure* **20,** 2124–2137; 10.1016/j.str.2012.09.018 (2012).

33. Blokesch, M. & Böck, A. Properties of the [NiFe]-hydrogenase maturation protein HypD. *FEBS Lett.* **580,** 4065–4068; 10.1016/j.febslet.2006.06.045 (2006).

34. Yang, X., Liu, Y., Gan, J., Xiao, Z.-X. & Cao, Y. FitDock: protein-ligand docking by template fitting. *Brief. Bioinform.* **23**; 10.1093/bib/bbac087 (2022).

35. Liu, Y. *et al.* CB-Dock2: improved protein-ligand blind docking by integrating cavity detection, docking and homologous template fitting. *Nucleic Acids Res.* **50,** W159-W164; 10.1093/nar/gkac394 (2022).

36. Tominaga, T. *et al.* Crystal structures of the carbamoylated and cyanated forms of HypE for [NiFe] hydrogenase maturation. *Proc. Natl. Acad. Sci. U. S. A.* **110,** 20485–20490; 10.1073/pnas.1313620110 (2013).

37. Watanabe, S. *et al.* Crystal structures of [NiFe] hydrogenase maturation proteins HypC, HypD, and HypE: insights into cyanation reaction by thiol redox signaling. *Mol.Cell* **27,** 29–40; 10.1016/j.molcel.2007.05.039 (2007).

38. Stripp, S. T. *et al.* HypD is the scaffold protein for Fe-$(CN)_2CO$ cofactor assembly in [NiFe]-hydrogenase maturation. *Biochemistry* **52,** 3289–3296; 10.1021/bi400302v (2013).

39. Piersimoni, L., Kastritis, P. L., Arlt, C. & Sinz, A. Cross-linking mass spectrometry for investigating protein conformations and protein-protein interactions─A method for all seasons. *Chem. Rev.* **122,** 7500–7531; 10.1021/acs.chemrev.1c00786 (2022).

40. Schneider, M., Belsom, A. & Rappsilber, J. Protein tertiary structure by crosslinking/mass spectrometry. *Trends Biochem. Sci.* **43,** 157–169; 10.1016/j.tibs.2017.12.006 (2018).

41. Leitner, A. *et al.* Toward increased reliability, transparency, and accessibility in cross-linking mass spectrometry. *Structure* **28,** 1259–1268; 10.1016/j.str.2020.09.011 (2020).

42. Lenz, S. *et al.* Reliable identification of protein-protein interactions by crosslinking mass spectrometry. *Nat. Commun.* **12,** 3564; 10.1038/s41467-021-23666-z (2021).

43. Merkley, E. D. *et al.* Distance restraints from crosslinking mass spectrometry: mining a molecular dynamics simulation database to evaluate lysine-lysine distances. *Protein Sci.* **23,** 747–759; 10.1002/pro.2458 (2014).

44. Abramson, J. *et al.* Accurate structure prediction of biomolecular interactions with AlphaFold 3. *Nature*; 10.1038/s41586-024-07487-w (2024).

45. Kwon, S. *et al.* Crystal structures of a [NiFe] hydrogenase large subunit HyhL in an immature state in complex with a Ni chaperone HypA. *Proc. Natl. Acad. Sci. U. S. A.* **115,** 7045–7050; 10.1073/pnas.1801955115 (2018).

46. Vaccaro, F. A. & Drennan, C. L. The role of nucleoside triphosphate hydrolase metallochaperones in making metalloenzymes. *Metallomics* **14**; 10.1093/mtomcs/mfac030 (2022).

47. Caserta, G. *et al.* Structural and functional characterization of the hydrogenase-maturation HydF protein. *Nat. Chem. Biol.* **13,** 779–784; 10.1038/nchembio.2385 (2017).

48. Yu, X., Rao, G., Britt, R. D. & Rauchfuss, T. B. Final stages in the biosynthesis of the [FeFe]-hydrogenase active site. *Angew. Chem. Int. Ed.* e202404044; 10.1002/anie.202404044 (2024).

49. Pagnier, A., Balci, B., Shepard, E. M., Broderick, W. E. & Broderick, J. B. [FeFe]-hydrogenase in vitro maturation. *Angew. Chem. Int. Ed.* **61,** e202212074; 10.1002/anie.202212074 (2022).

50. Brawley, H. N., Kreinbrink, A. C., Hierholzer, J. D., Vali, S. W. & Lindahl, P. A. Labile iron pool of isolated *Escherichia coli* cytosol likely includes Fe-ATP and Fe-Citrate but

not Fe-Glutathione or aqueous Fe. *J. Am. Chem. Soc.* **145,** 2104–2117; 10.1021/jacs.2c06625 (2023).

51. Kornberg, A. & Pricer, W. E. Enzymatic phosphorylation of adenosine and 2,6-diaminopuridine riboside. *J. Biol. Chem.* **193,** 481–495; 10.1016/s0021-9258(18)50904-2 (1951).

52. Bergmeyer, H. U. Neue Werte für die molaren Extinktions-Koeffizienten von NADH und NADPH zum Gebrauch im Routine-Laboratorium. *Das Medizinische Laboratorium* **30,** 57–59 (1977).

53. Gee, L. B., Wang, H. & Cramer, S. P. NRVS for Fe in biology: experiment and basic interpretation. *Methods Enzymol.* **599**, 409–425; 10.1016/bs.mie.2017.11.002 (2018).

54. Doellinger, J., Schneider, A., Hoeller, M. & Lasch, P. Sample preparation by easy extraction and digestion (SPEED) - A universal, rapid, and detergent-free protocol for proteomics based on acid extraction. *Mol. Cell. Proteomics* **19,** 209–222; 10.1074/mcp.TIR119.001616 (2020).

55. Rappsilber, J., Mann, M. & Ishihama, Y. Protocol for micro-purification, enrichment, pre-fractionation and storage of peptides for proteomics using StageTips. *Nat. Protoc.* **2,** 1896–1906; 10.1038/nprot.2007.261 (2007).

56. Mendes, M. L. *et al.* An integrated workflow for crosslinking mass spectrometry. *Mol. Syst. Biol.* **15,** e8994; 10.15252/msb.20198994 (2019).

57. Mirdita, M. *et al.* ColabFold: making protein folding accessible to all. *Nat. Methods* **19,** 679–682; 10.1038/s41592-022-01488-1 (2022).

58. Jumper, J. *et al.* Highly accurate protein structure prediction with AlphaFold. *Nature* **596,** 583–589; 10.1038/s41586-021-03819-2 (2021).

59. Kim, G. *et al. Easy and accurate protein structure prediction using ColabFold* (2023).

60. Schrodinger L. L. C. The PyMOL molecular graphics system. *Version* **1,** 8 (2015).

61. Fritsch, J. *et al.* The crystal structure of an oxygen-tolerant hydrogenase uncovers a novel iron-sulphur centre. *Nature* **479,** 249–252; 10.1038/nature10505 (2011).

62. Pelmenschikov, V., Blomberg, M. R. A. & Siegbahn, P. E. M. A theoretical study of the mechanism for peptide hydrolysis by thermolysin. *J. Biol. Inorg. Chem.* **7,** 284–298; 10.1007/s007750100295 (2002).

63. Frisch, M. J. *et al. Gaussian 16 Rev. C.01* (Wallingford, CT, 2016).

64. Bochevarov, A. D. *et al.* Jaguar: A high-performance quantum chemistry software program with strengths in life and materials sciences. *Int. J. Quantum Chem.* **113,** 2110–2142; 10.1002/qua.24481 (2013).

65. Adamo, C. & Barone, V. Toward reliable density functional methods without adjustable parameters: The PBE0 model. *J. Chem Phys.* **110,** 6158–6170; 10.1063/1.478522 (1999).

66. Krishnan, R., Binkley, J. S., Seeger, R. & Pople, J. A. Self-consistent molecular orbital methods. XX. A basis set for correlated wave functions. *J. Chem Phys.* **72,** 650–654; 10.1063/1.438955 (1980).

67. McLean, A. D. & Chandler, G. S. Contracted Gaussian basis sets for molecular calculations. I. Second row atoms, Z =11–18. *J. Chem Phys.* **72,** 5639–5648; 10.1063/1.438980 (1980).

68. Tomasi, J., Mennucci, B. & Cammi, R. Quantum mechanical continuum solvation models. *Chem. Rev.* **105,** 2999–3093; 10.1021/cr9904009 (2005).

69. Pelmenschikov, V., Guo, Y., Wang, H., Cramer, S. P. & Case, D. A. Fe-H/D stretching and bending modes in nuclear resonant vibrational, Raman and infrared spectroscopies: comparisons of density functional theory and experiment. *Farad. Disc.* **148,** 409-20; discussion 421-41; 10.1039/c004367m (2011).